Flows in the Convection Zone with Potential Relevance to the Sunspot Problem

Tom Duvall
MPS Gottingen

So, what are these flows?

- Depth structure of supergranules.
- Convection in the outer third of the convection zone. (Hanasoge et al. 2010; Hanasoge et al. 2013)
- Vorticity in the supergranulation. (Langfellner, Gizon, Birch, 2014; 2015)

Average Dopplergram Minus Polynomial Fit

45 images averaged (30-Mar-96 19:26 to 30-Mar-96 20:17)

SOI / MDI

Stanford Lockheed Institute for Space Research

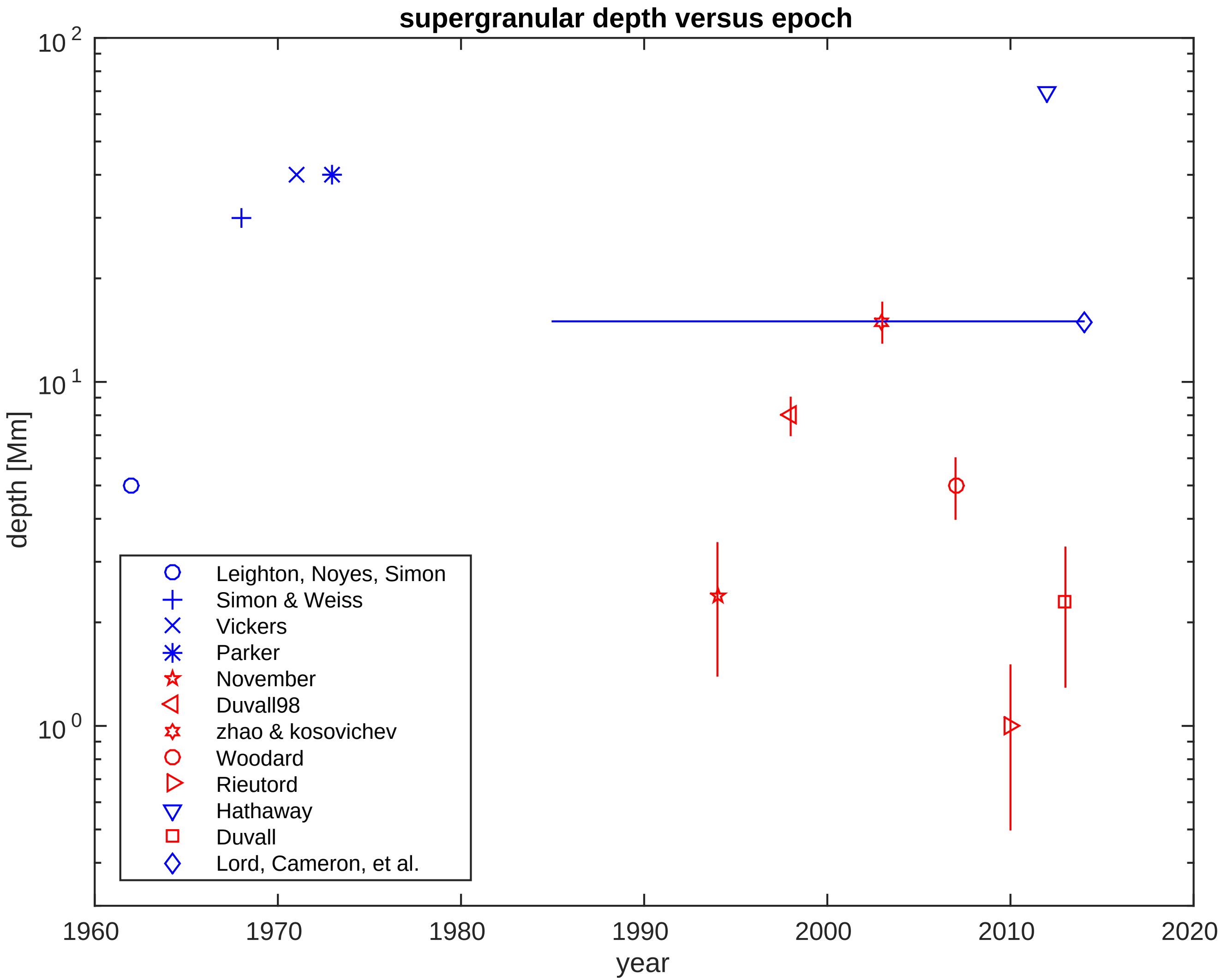
supergranular depth versus epoch
depth [Mm]
10^2
10^1
10^0
1960
1970
1980
1990
2000
2010
2020
year
Leighton, Noyes, Simon
Simon & Weiss
Vickers
Parker
November
Duvall98
zhao & kosovichev
Woodard
Rieutord
Hathaway
Duvall
Lord, Cameron, et al.

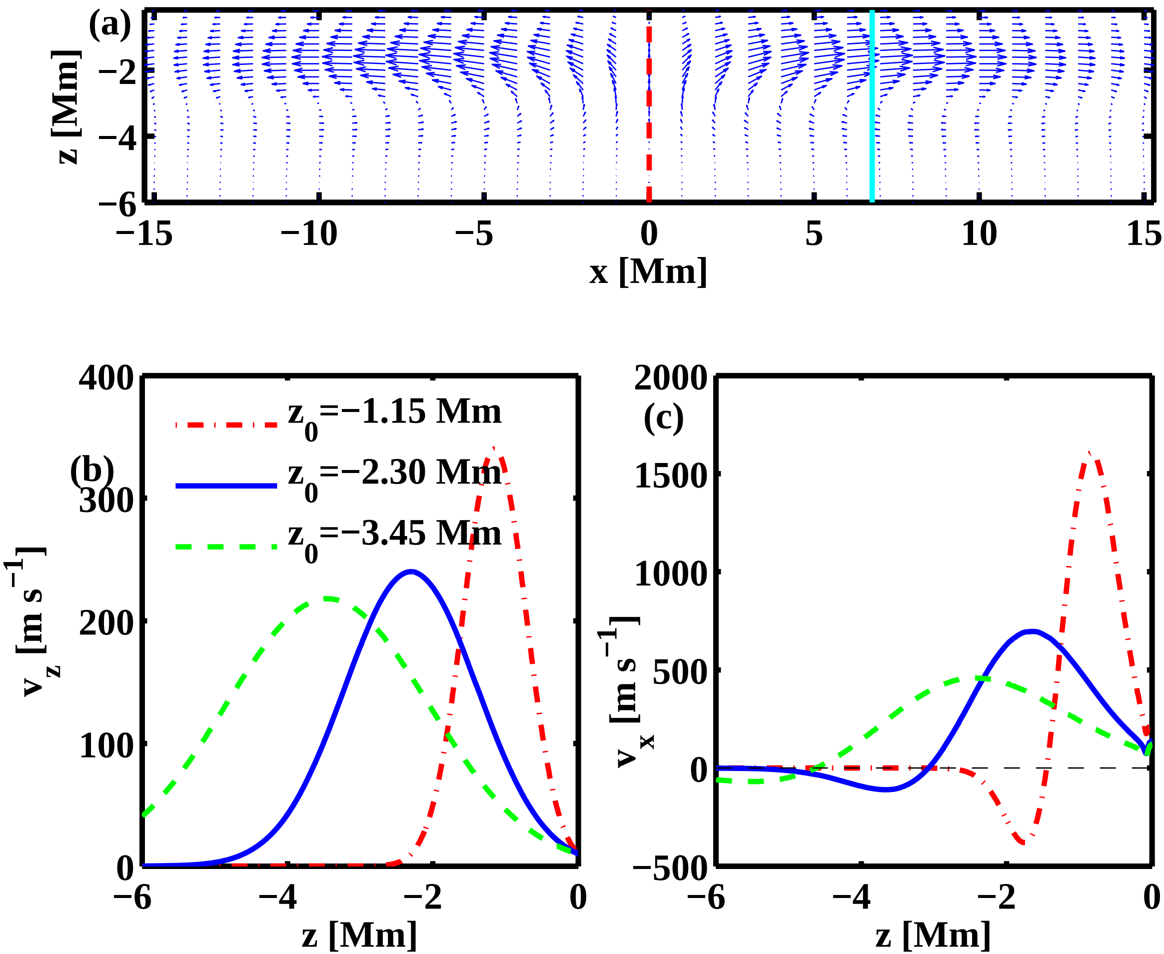

(a)
z [Mm]
−2
−4
−6
−15
−10
−5
0
5
10
15
x [Mm]
(b)
400
300
200
100
0
v_z [m s^−1]
−6
−4
−2
0
z [Mm]
z_0=−1.15 Mm
z_0=−2.30 Mm
z_0=−3.45 Mm
(c)
2000
1500
1000
500
0
−500
v_x [m s^−1]
−6
−4
−2
0
z [Mm]

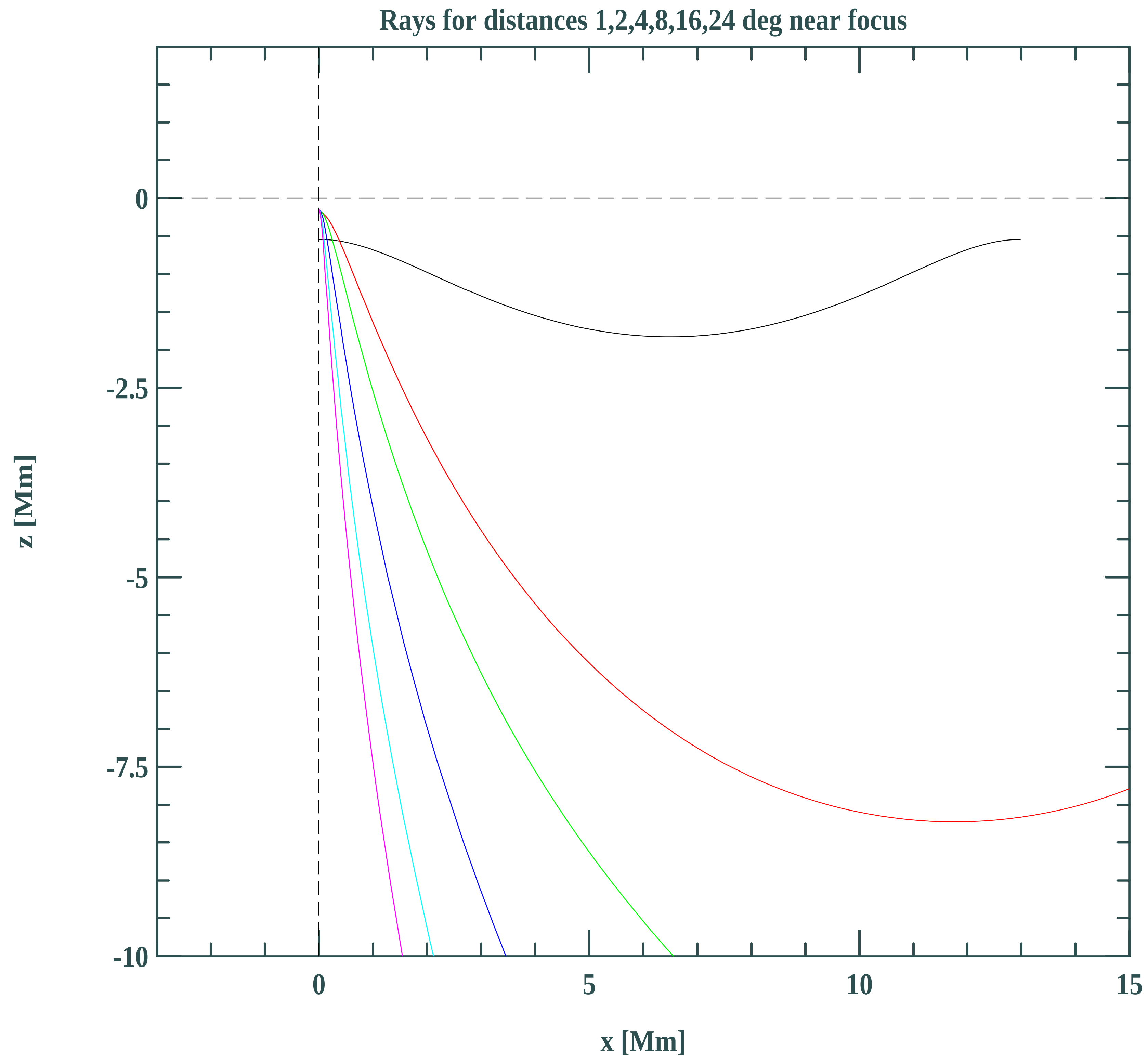
Rays for distances 1,2,4,8,16,24 deg near focus
z [Mm]
x [Mm]
0
-2.5
-5
-7.5
-10
0
5
10
15

Surface-focused rays for distances 1,2,4,8,16,24 deg.

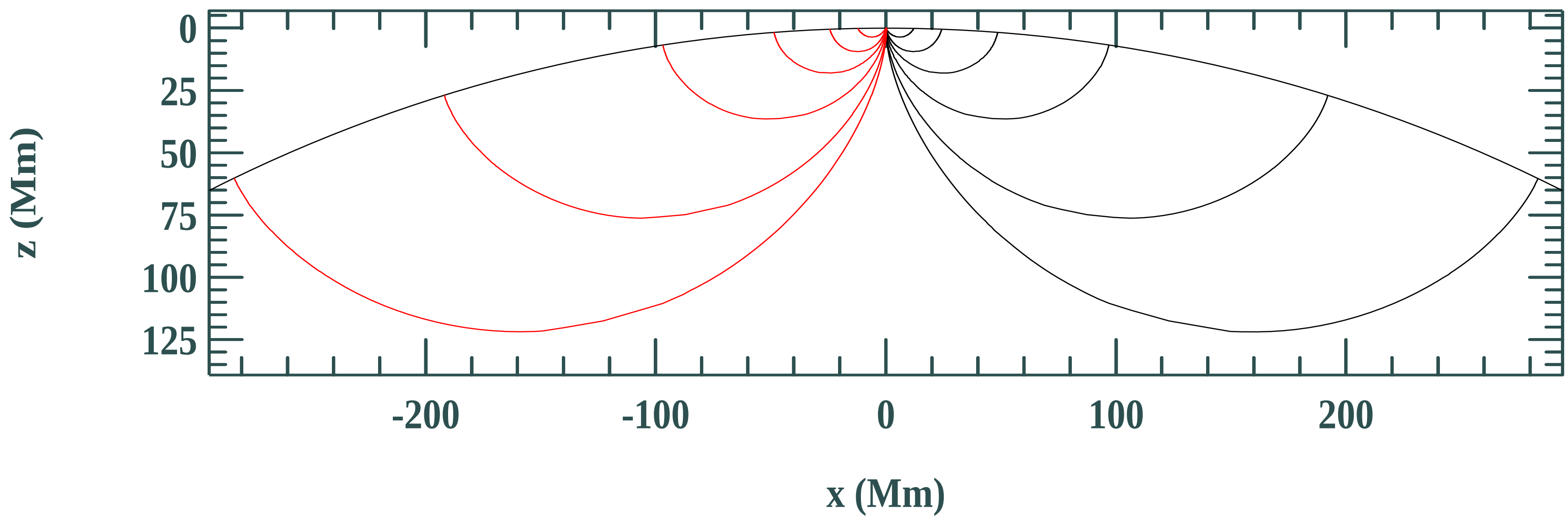

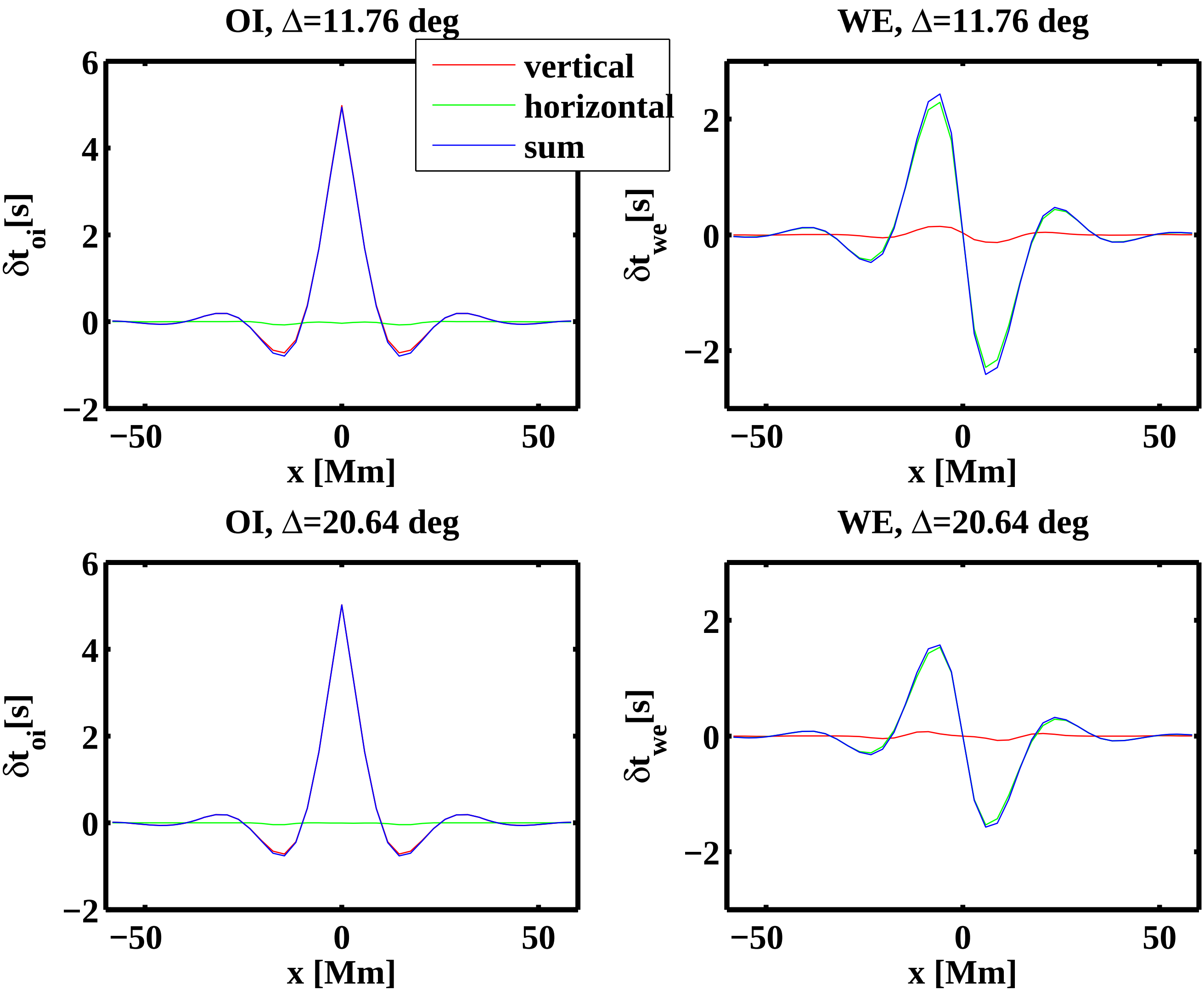

OI, Δ=11.76 deg
WE, Δ=11.76 deg
OI, Δ=20.64 deg
WE, Δ=20.64 deg
vertical
horizontal
sum
δt_oi [s]
δt_we [s]
x [Mm]
6
4
2
0
−2
−50
50

F-mode divergence signal with feature locations overlaid in red.

- Supergranule location: First an f-mode analysis is done to 'find' the supergranules. Maps of the travel time difference between the inward-going waves and outward-going waves from a central point to an annulus yield a signal proportional to the horizontal divergence. Local peaks in this signal define the location of the centers of the supergranular cells. 64 12-hour intervals were analyzed yielding 60000 supergranules to use.

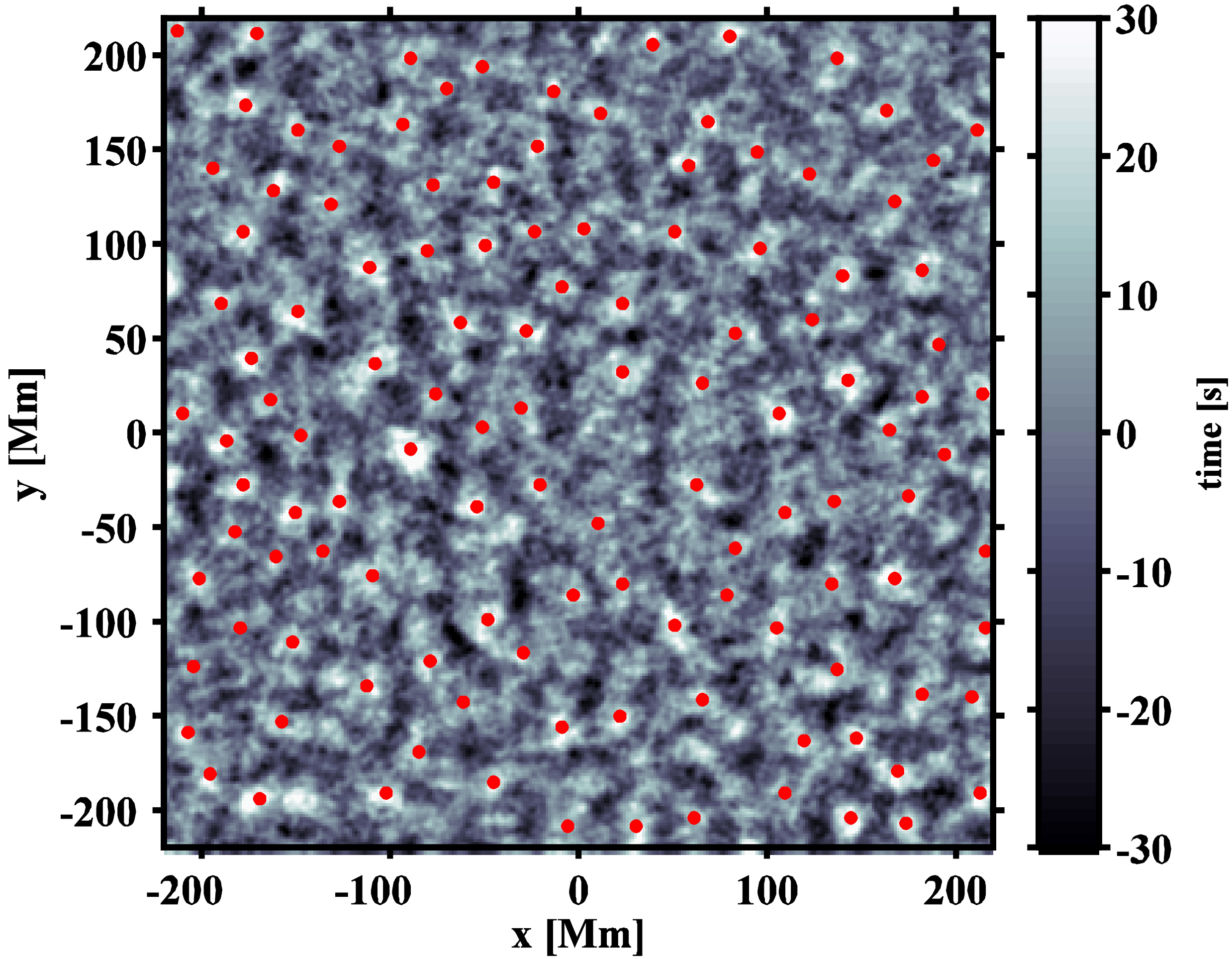

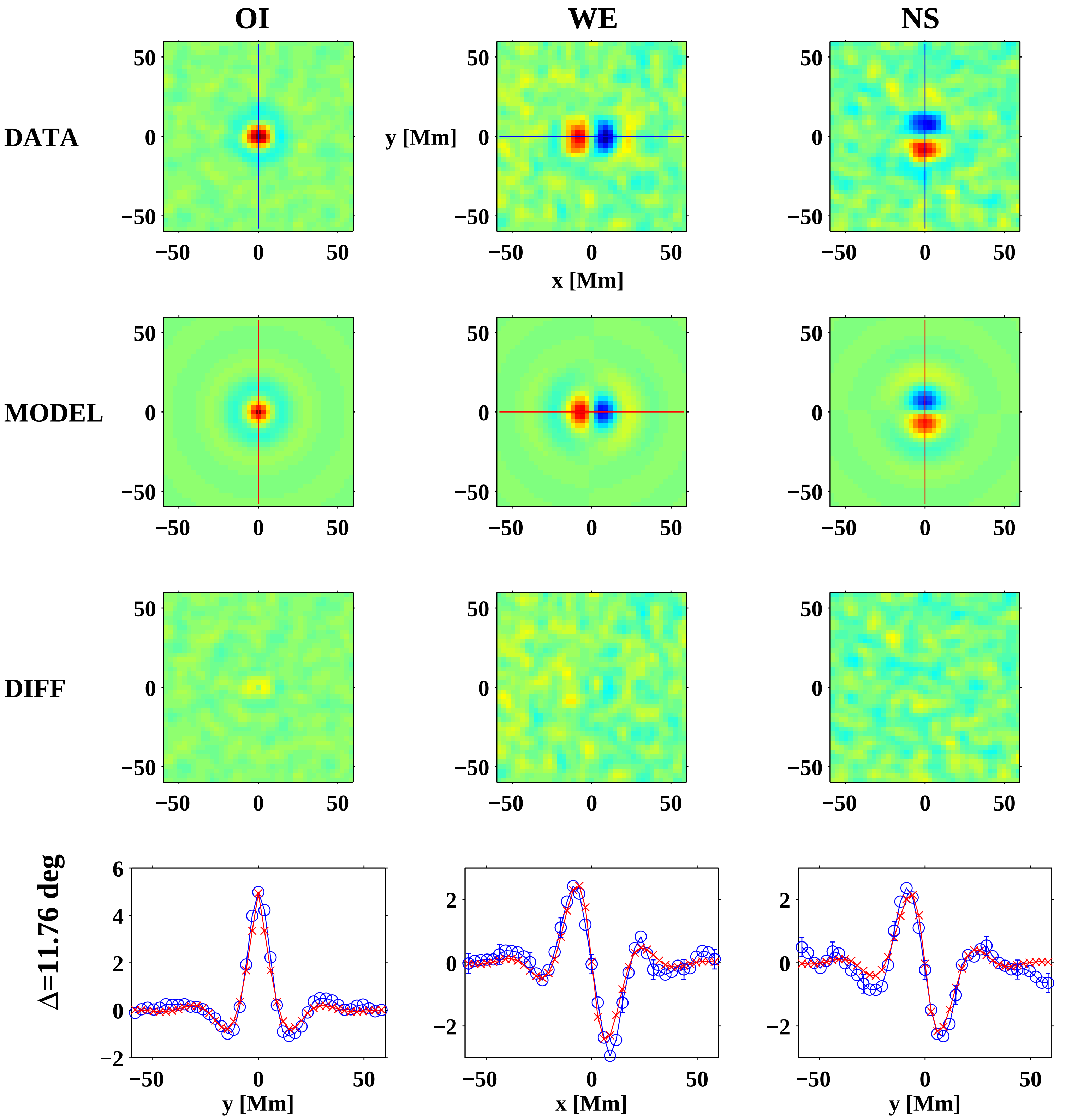

OI
WE
NS
DATA
MODEL
DIFF
Δ=11.76 deg
y [Mm]
x [Mm]

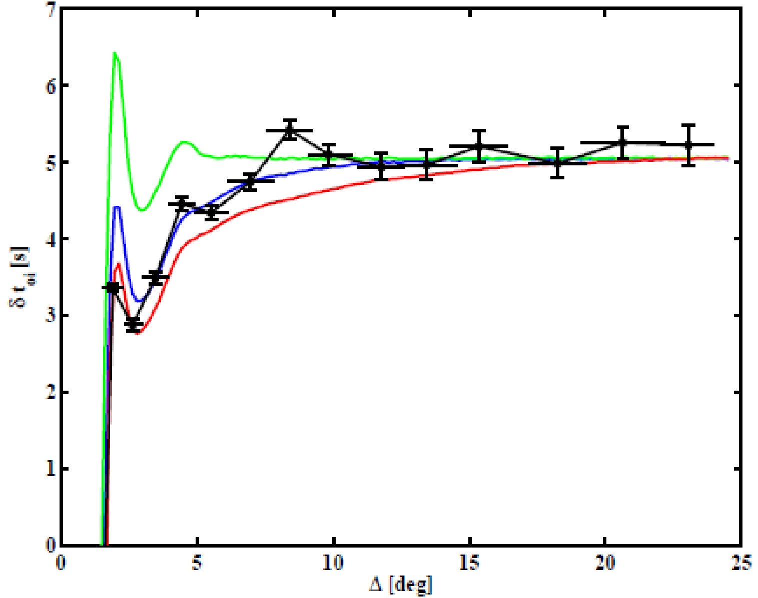

Figure 6. Comparison of the three ray models from Figure 1 with the HMI results (black) of the $\Gamma_\ell = 400$ filtering and the Gabor-wavelet phase speed time differences from Figure 5(d). These models are the sum of vertical and horizontal signals for the three Gaussian vertical flows peaking at $z_0 = -3.45\,\mathrm{Mm}$ (red), $z_0 = -2.3\,\mathrm{Mm}$ (blue), and $z_0 = -1.15\,\mathrm{Mm}$ (green) specified in Table 1.

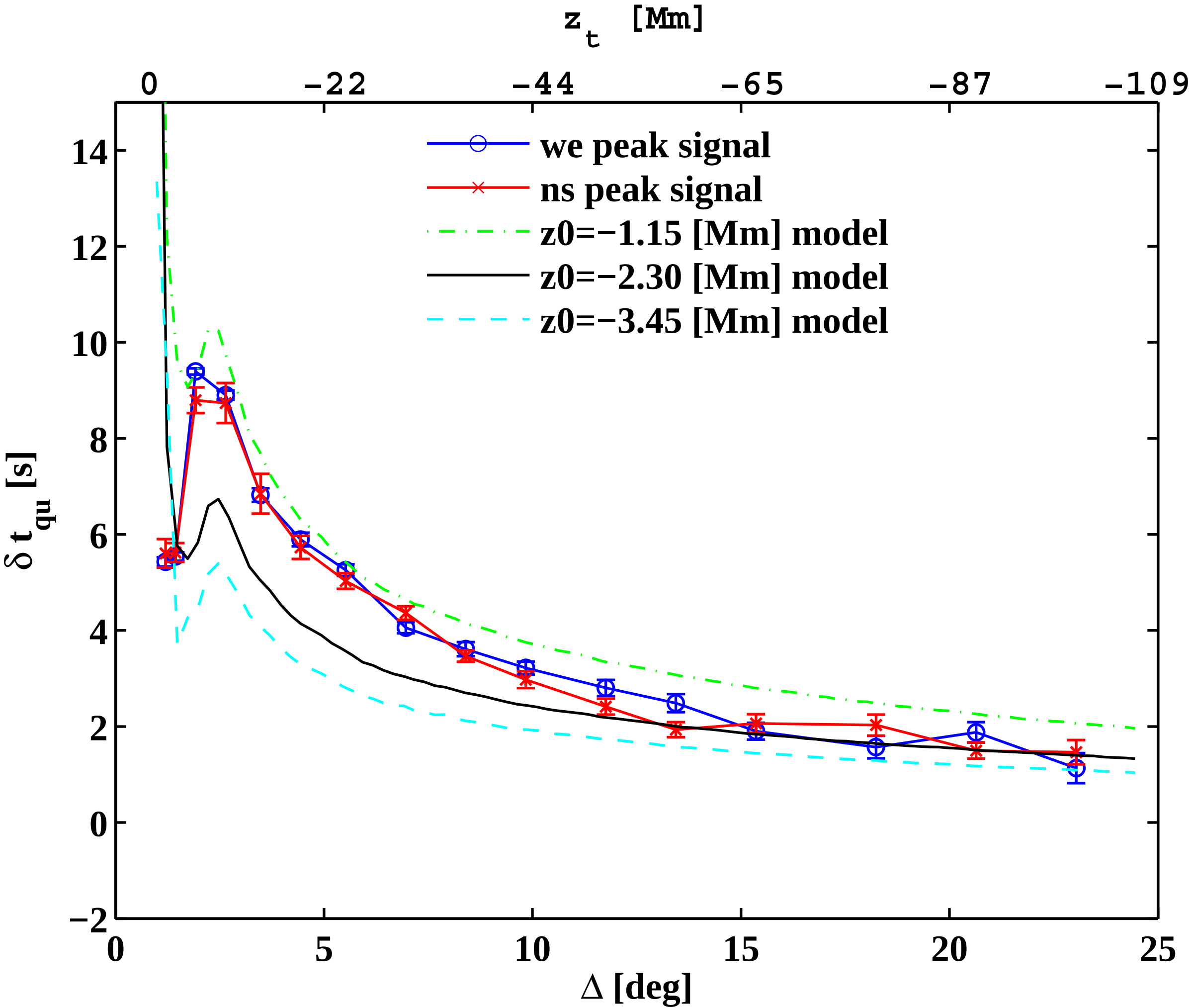

z_t [Mm]
0
−22
−44
−65
−87
−109
we peak signal
ns peak signal
z0=−1.15 [Mm] model
z0=−2.30 [Mm] model
z0=−3.45 [Mm] model
δt_{qu} [s]
14
12
10
8
6
4
2
0
−2
0
5
10
15
20
25
Δ [deg]

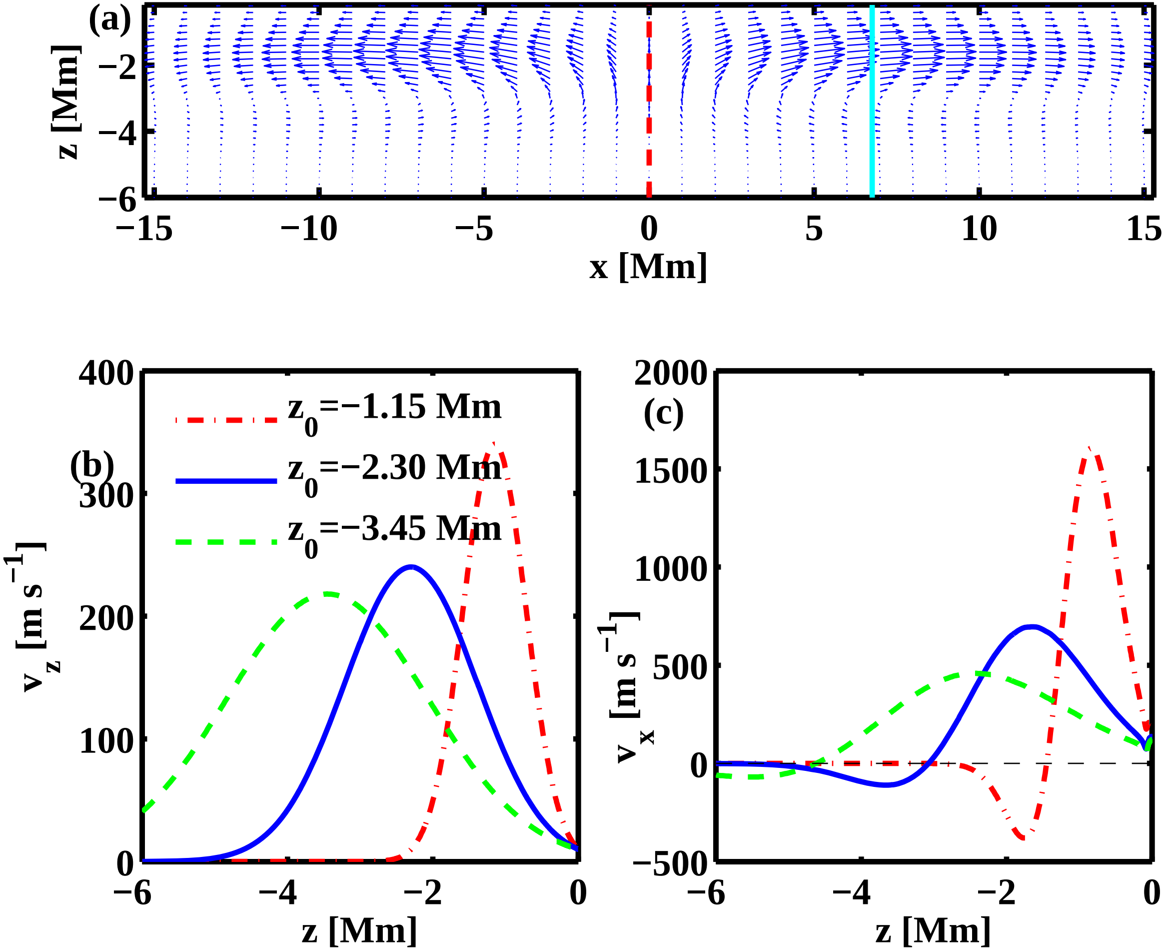

(a)
z [Mm]
−2
−4
−6
−15
−10
−5
0
5
10
15
x [Mm]
(b)
z_0=−1.15 Mm
z_0=−2.30 Mm
z_0=−3.45 Mm
400
300
200
100
0
v_z [m s^{-1}]
−6
−4
−2
0
z [Mm]
(c)
2000
1500
1000
500
0
−500
v_x [m s^{-1}]
−6
−4
−2
0
z [Mm]

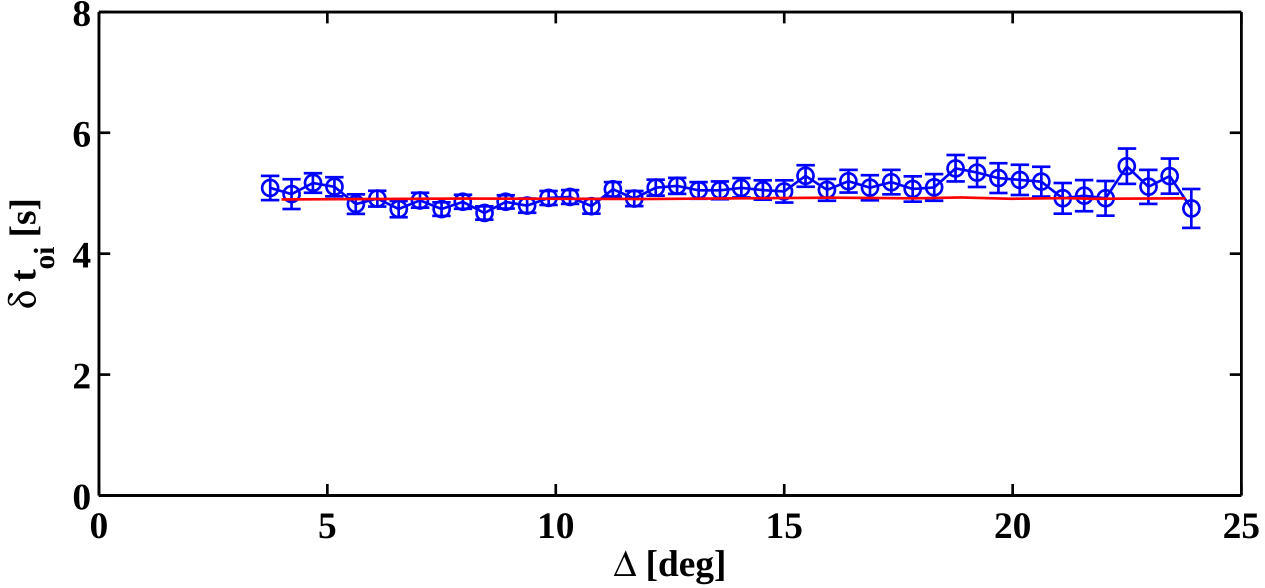

8
6
4
2
0
δt_{oi} [s]
0
5
10
15
20
25
Δ [deg]

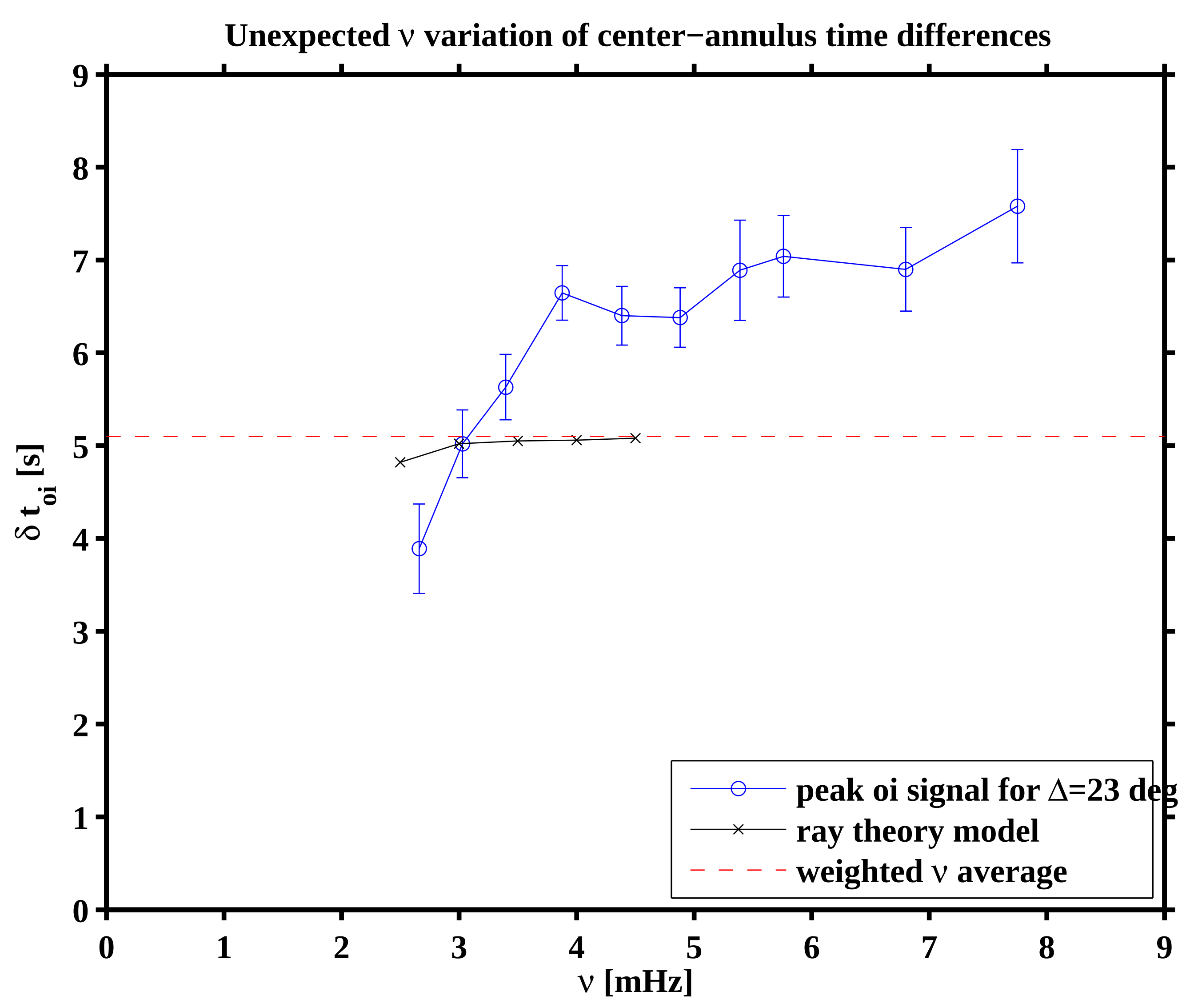

Unexpected ν variation of center−annulus time differences
δ t_oi [s]
ν [mHz]
0
1
2
3
4
5
6
7
8
9
peak oi signal for Δ=23 deg
ray theory model
weighted ν average

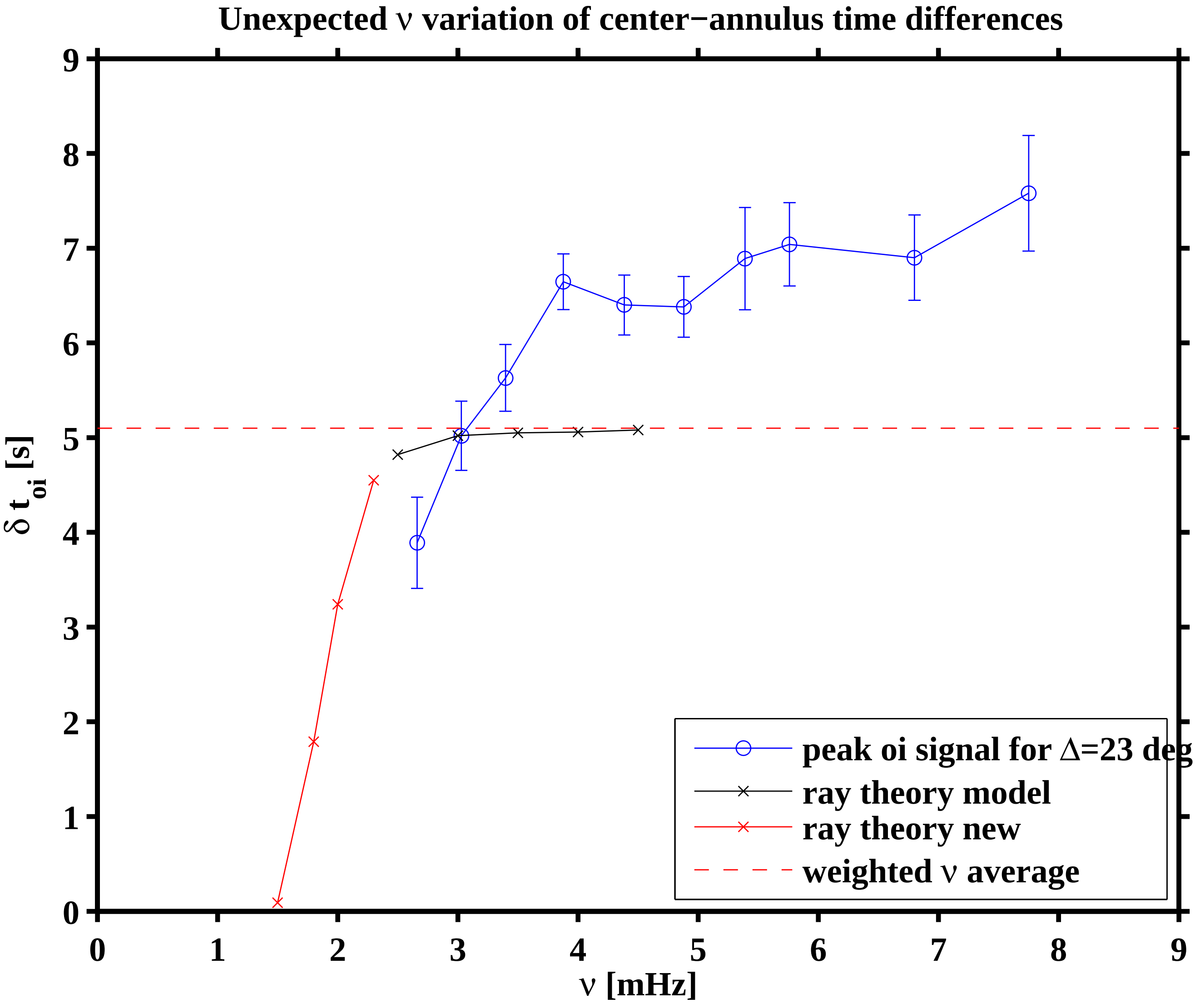

Unexpected ν variation of center−annulus time differences
δ t_oi [s]
ν [mHz]
0
1
2
3
4
5
6
7
8
9
peak oi signal for Δ=23 deg
ray theory model
ray theory new
weighted ν average

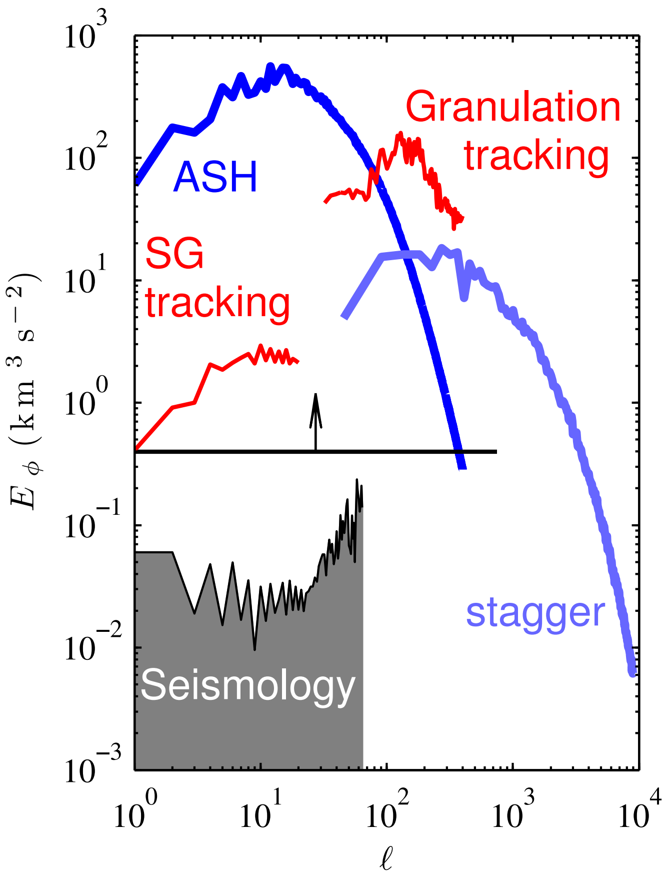

Figure 5

Upper bounds on kinetic energy E_ϕ of longitudinal velocities v_ϕ versus spherical-harmonic degree, ℓ. We define E_ϕ at radius r such that $\langle v_\phi^2 \rangle/2 = \sum_{\ell \geq 0} E_\phi(\ell)/r$, where the expectation value is approximated by a horizontal average. The grey region shows the helioseismology bound, based on $T = 96$-hour samples of HMI observations (Hanasoge, Duvall & Sreenivasan 2012). These constraints are several orders in magnitude smaller than numerical simulations of global convection (Anelastic Spherical Harmonic simulation: ASH; Miesch et al. 2009), suggesting that our current modeling of large-scale convection in the Sun is incomplete. The various curves denote convective energy spectra at different depths: seismology corresponds to $r/R_\odot = 0.96$, ASH to $r/R_\odot = 0.97$, and Stagger simulations to $r/R_\odot = 0.98$. The horizontal black line is a theoretical lower bound based on global dynamics arguments Miesch et al. (2012), assuming mode equipartition over $\ell < 750$. The red curves are surface spectra based on HMI observations of granulation and supergranulation (SG) tracking. The SG tracking spectrum is based on data from Hathaway, Upton & Colegrove (2013), courtesy of David Hathaway. Adapted from Gizon & Birch (2012).

Something is missing from our current theoretical understanding of solar convection below ~ 10 Mm". Of particular relevance to models of convection are the matching of the amplitude of convective motions at all scales at the surface and accurately matching the ratios of power spectra at different depths. Both of these factors are strong tests of the mechanism

Figure 1. CITED IN TEXT | HIGH RESOLUTION IMAGE Go to: Figure 2.

Pictorial representation of deep-focusing time-distance helioseismology. Numerous waves, denoted here by rays, that intersect at $r/R_\odot = 0.95$ are utilized in order to image flows at that depth (shown by the horizontal curved dashed line) and that horizontal location. The signal associated with the waves is measured at the solar photosphere (depicted by the horizontal curved solid line).

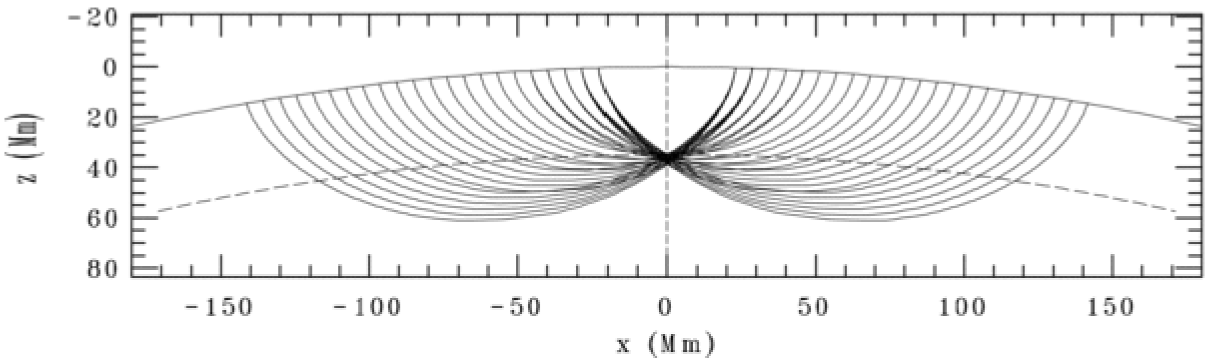

Figure 3. CITED IN TEXT | HIGH RESOLUTION IMAGE Go to: Figure 2. | Figure 4.

Comparison of flows at a depth of $r/R_\odot = 0.95$ and deep-focus travel-time differences (configuration shown in Figure 1). The left column shows the flows from the simulation: from top to bottom, the radial (v_r), north-south (v_λ), and east-west (v_ϕ) components at $r/R_\odot = 0.95$. Travel-time differences corresponding to these three components are shown on the right-hand column: from top to bottom, the difference between the ingoing and outgoing travel times (τ_{io}), the north-south travel-time asymmetry (τ_{ns}), and the east-west travel-time asymmetry (τ_{ew}). The correlation coefficients between the flows and travel-time maps are 0.17 for the radial, 0.59 for the north-south, and 0.69 for the east-west cases. The spatial cross-correlations between the travel-time and velocity maps have a FWHM of 9° for both the north-south and east-west cases.

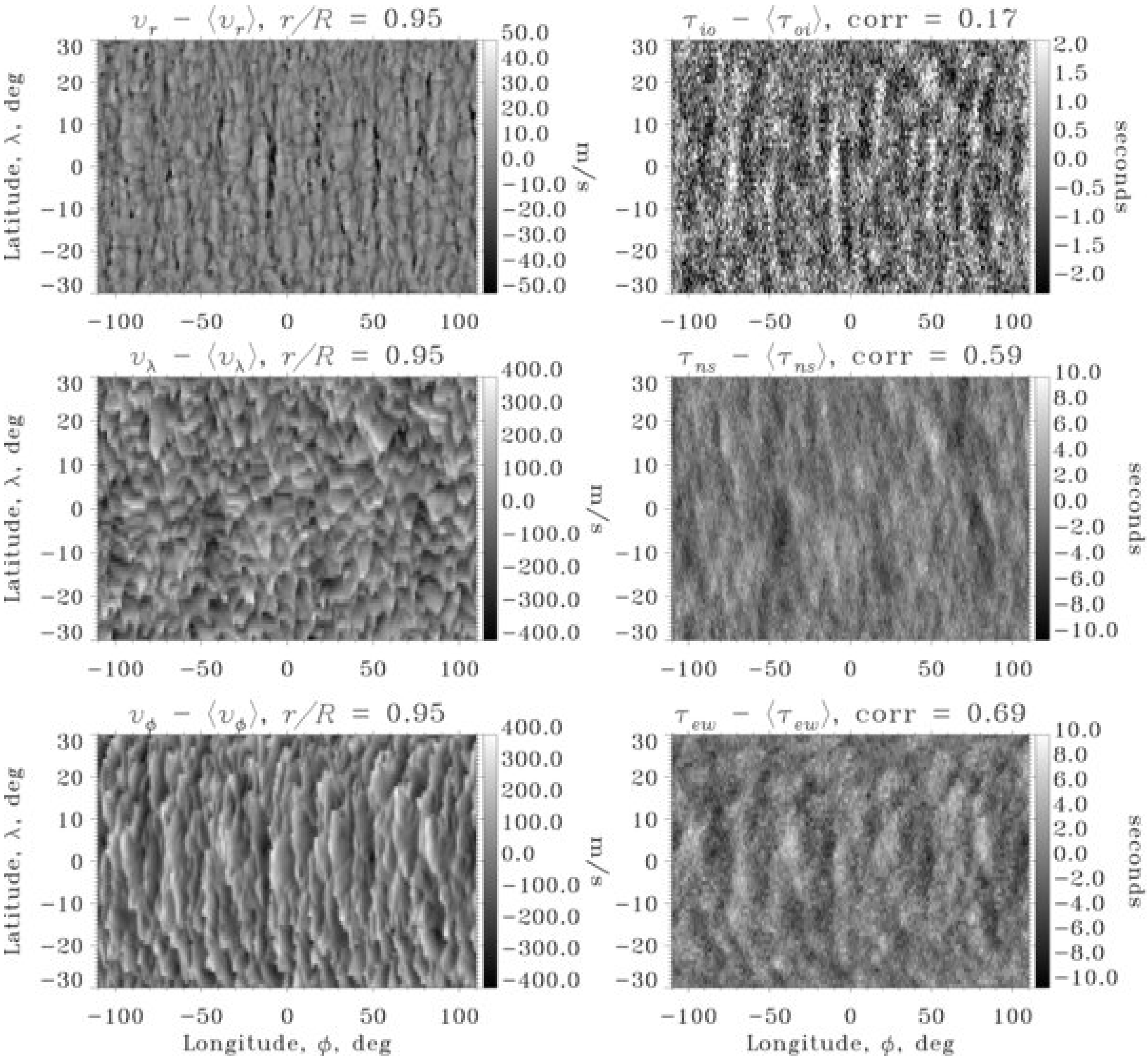

Figure 4. CITED IN TEXT | HIGH RESOLUTION IMAGE Go to: Figure 3. | Figure 5.

Measure of the imaging resolution of helioseismic waves. For example, a convective cell with horizontal velocity amplitude 100 m s^{-1} and dominant spatial power in $\ell = 1$ will elicit approximately a 3 s shift in the travel times as measured by this deep-focusing technique. Similar interpretations apply to convective features at higher ℓ. Finer-scale features at this depth, i.e., those characterized by $\ell > 50$, register much more weakly in the travel times. Note that these curves suggest an imaging resolution of $\ell \sim 30$ (defined as the half-width), far smaller than the largest wavenumber ($\ell_{max} \sim 185$) that propagates at this depth ($r/R_\odot = 0.95$).

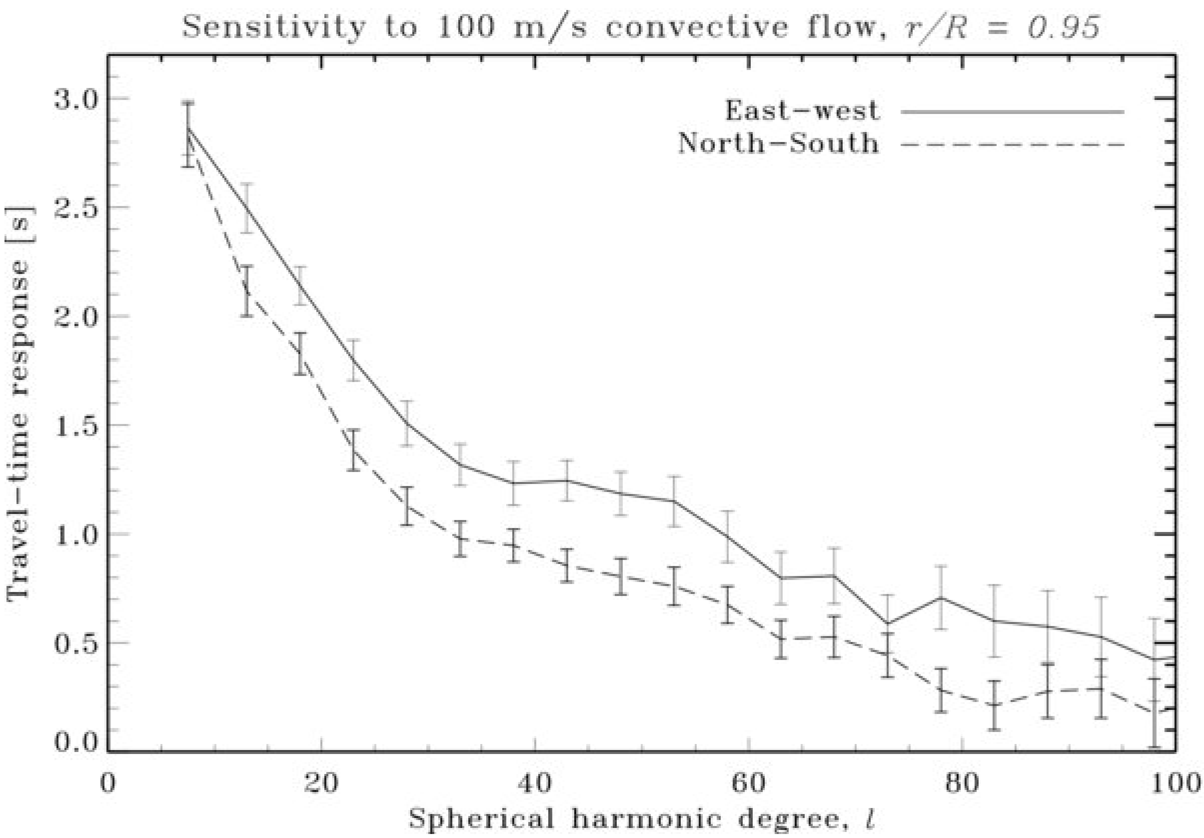

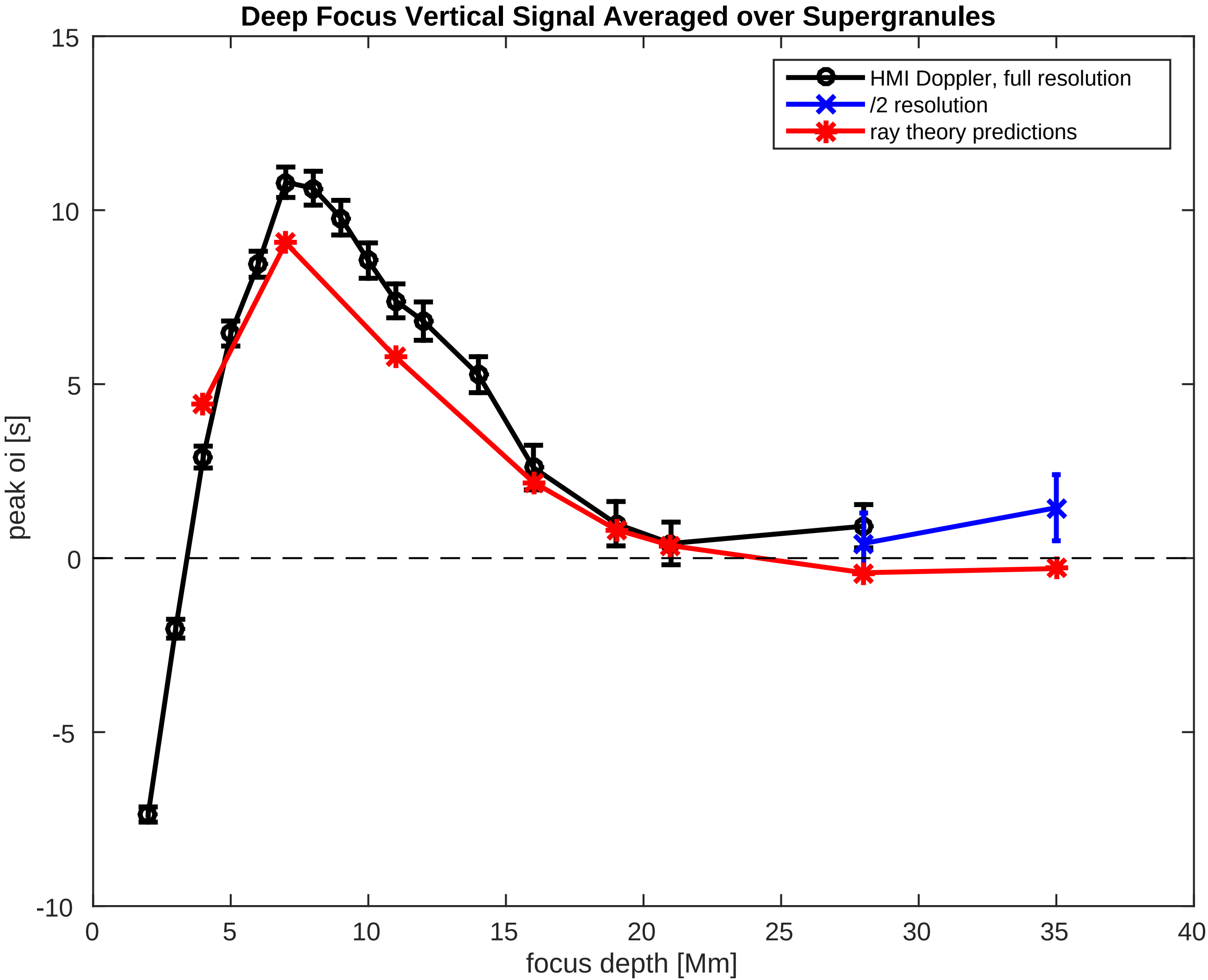

Deep Focus Vertical Signal Averaged over Supergranules
HMI Doppler, full resolution
/2 resolution
ray theory predictions
peak oi [s]
focus depth [Mm]
15
10
5
0
-5
-10
0
5
10
15
20
25
30
35
40

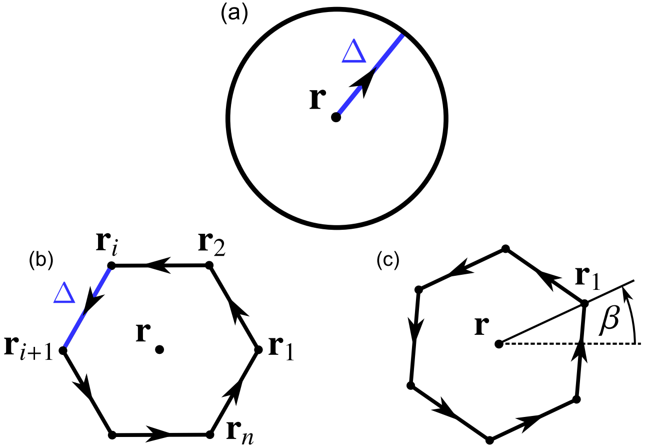

Fig. 1. Travel-time measurement geometries. **a)** Measurement geometry sensitive to the horizontal component of the flow divergence. Travel times are measured between a central point $\boldsymbol{r}$ and the average over a surrounding annulus with radius Δ as introduced by Duvall et al. (1993). **b)** Proposed new measurement geometry sensitive to the vertical component of flow vorticity. Travel times are measured sequentially along neighboring pairs of points $\boldsymbol{r}_i$ and $\boldsymbol{r}_{i+1}$ located on a closed contour. In this example, $n = 6$ points are used, forming a regular hexagon. **c)** As **b)**, but the hexagon is rotated by an angle β around $\boldsymbol{r}$.

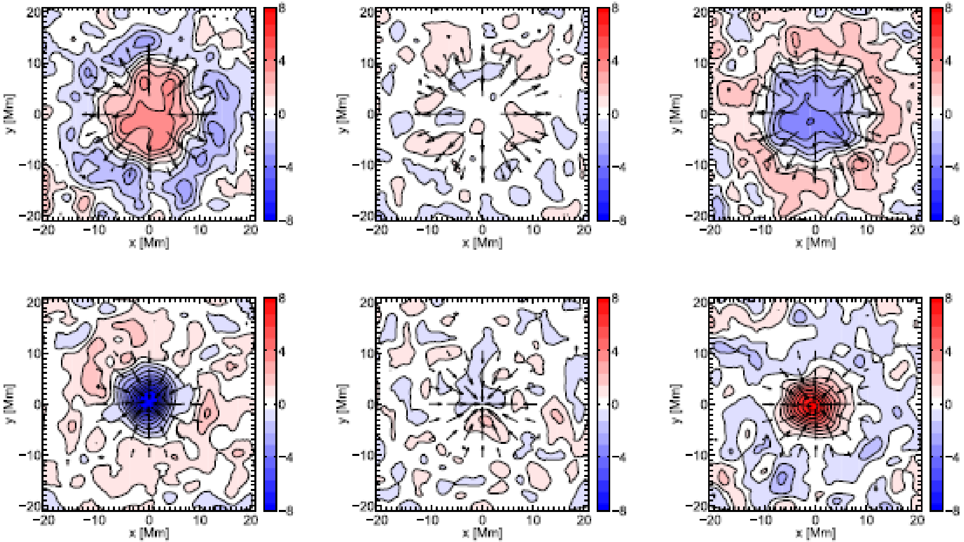

Figure 8

Vertical vorticity of the average supergranule in units of 10^{-6} s^{-1} at latitudes $-40°$, $0°$, and $+40°$ (from left to right) from local correlation tracking analysis. The colors refer to the radial component of vorticity, the arrows to the horizontal flow components. The top row is for outflows, the bottom row for inflows. Adapted from Langfellner, Gizon & Birch (2015).

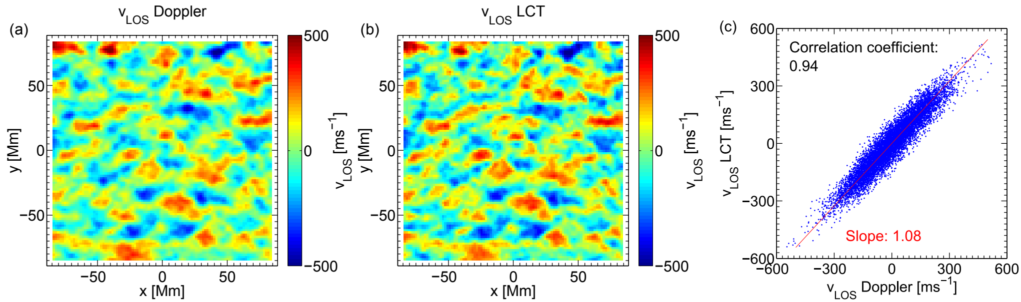

Fig. 2. Comparison of line-of-sight velocity from two different data products at 40° solar latitude. **a)** HMI Dopplergram averaged over 8 h. The map has been convolved with a Gaussian of $\sigma/\sqrt{2} \approx 1.4$ Mm and subsampled to match the coarser LCT resolution. The mean over the map and a linear function in the x direction (parameters determined by a least-squares fit) have been subtracted. **b)** LCT map from HMI intensity images, averaged over 8 h. The line-of-sight velocity component was computed from the v_x and v_y components. For v_y, the mean over the map and a linear function in y direction have been subtracted. **c)** Scatter plot of the two maps. The Pearson correlation coefficient is 0.94. The red line shows the direction of largest scatter and crosses the origin. It is a best-fit line in the sense that it minimizes the sum of squared distances of the points perpendicular to the line (cf. Pearson 1901). This is different from linear regression, where no error in the x coordinate is assumed and only the sum of squared distances in the vertical direction is minimized. The slope of the red line is 1.08; the error in the direction of lowest scatter is 33.9 m s^{-1}.

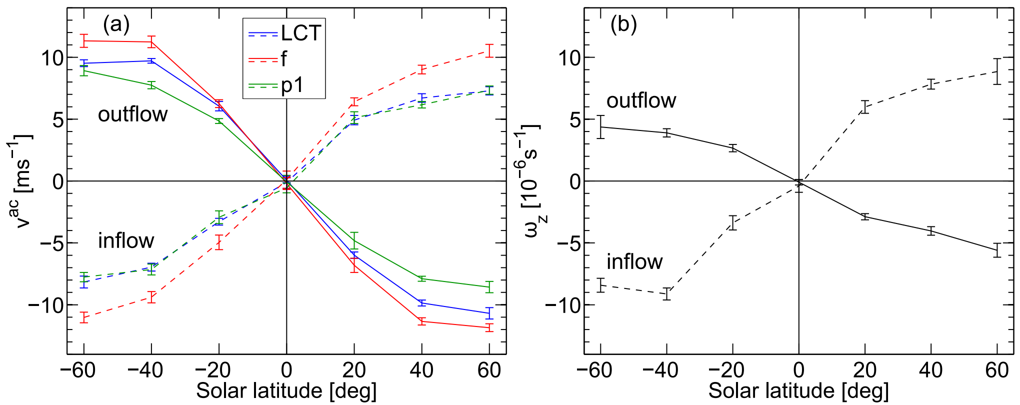

Fig. 8. Peak v^{ac} and ω_z values for the average supergranule at different solar latitudes. **a)** v^{ac} for LCT, f modes and p_1 modes. **b)** Vertical component of flow vorticity ω_z. Solid lines are for the average supergranule outflow region, dashed lines for the average supergranule inflow region. At 0° latitude, the values at the map center are shown instead of the peak values. The errors have been computed from dividing the 336 datasets into eight parts à 42 datasets and measuring the variance of v^{ac} and ω_z at the peak positions over the eight parts.

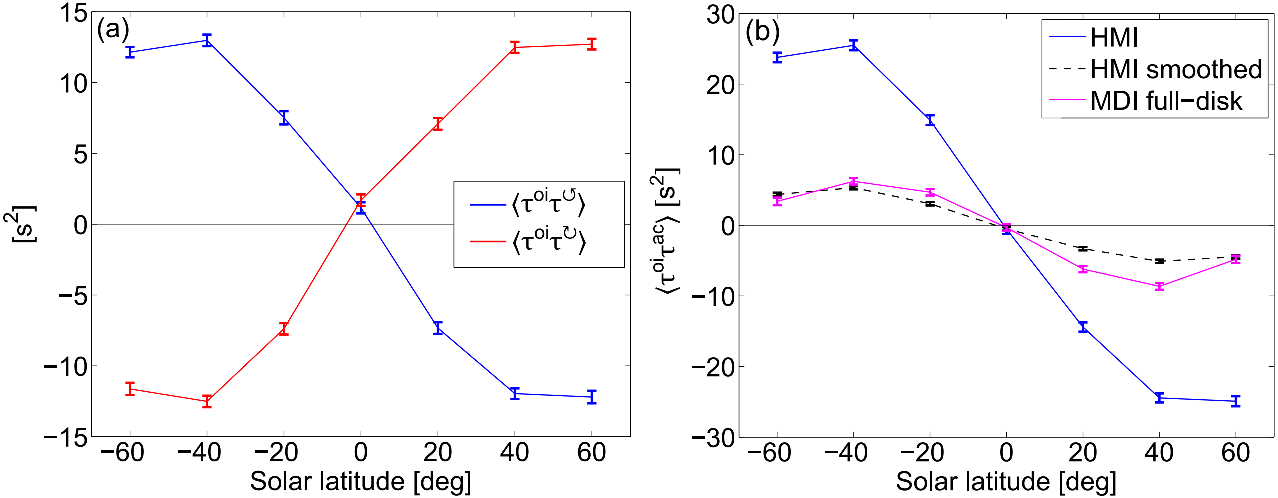

Fig. 5. a) Horizontal averages $\langle\tau^{oi}\tau^{\circlearrowleft}\rangle$ and $\langle\tau^{oi}\tau^{\circlearrowright}\rangle$ for f-mode-filtered HMI observations as functions of solar latitude, averaged over 336×8 h datasets of about 180×180 Mm^2 and four angles β. **b)** Horizontal average $\langle\tau^{oi}\tau^{ac}\rangle$ for different data: HMI at full resolution (0.5 arcsec px^{-1}), MDI full-disk data (2.0 arcsec px^{-1}), and HMI data spatially averaged over 4×4 px (after remapping) and convolved with a Gaussian with 2.4 Mm FWHM to match the MDI sampling and PSF.

Conclusions

- Depth and flow structure of supergranules still an interesting problem.
- Convection deeper into the Sun also needs more work.
- Rotation’s influence on convection has been measured clearly near the photosphere.

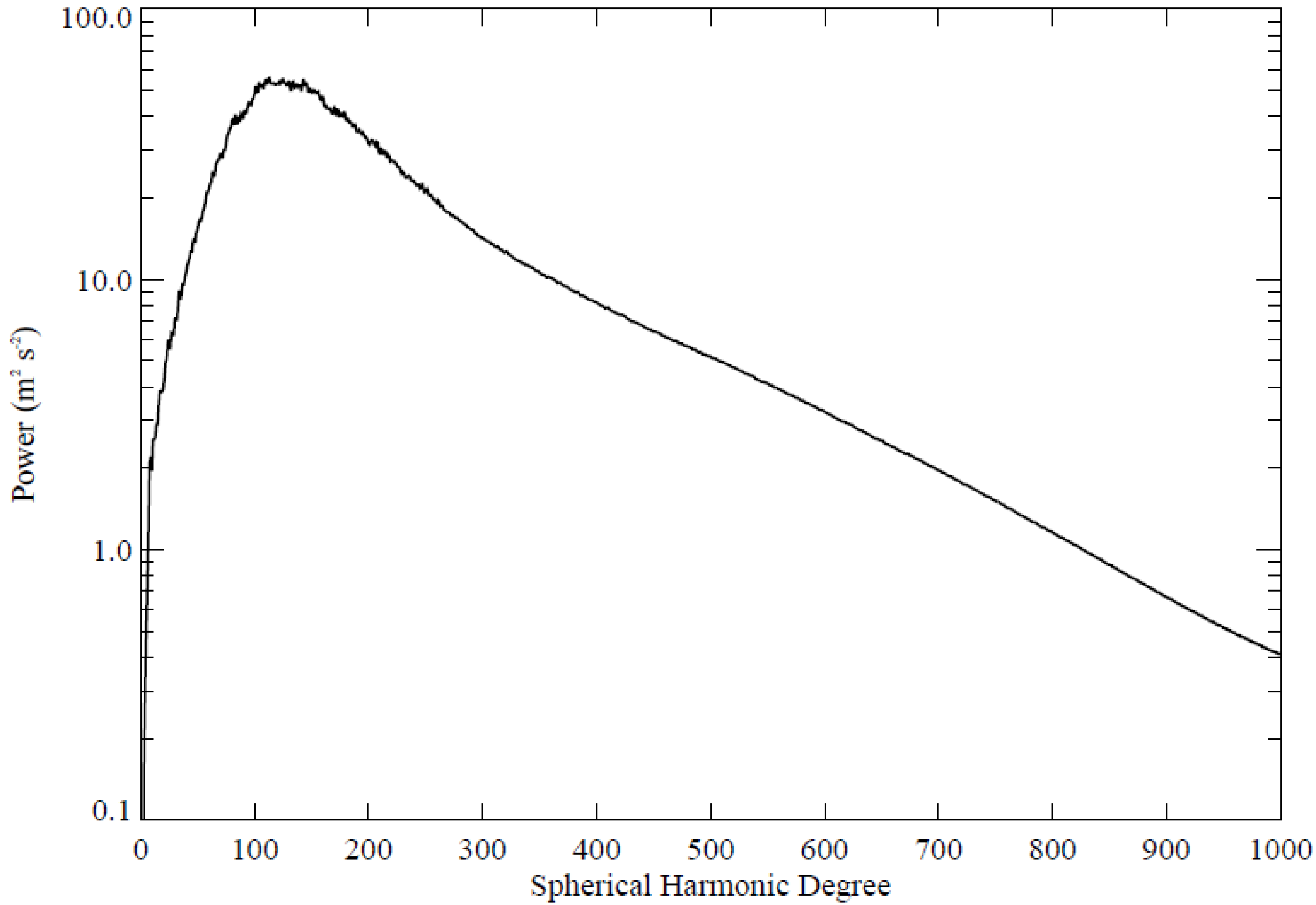

Figure 3. The average observed power spectrum for the cellular photospheric flows in the full-disk MDI data. The peak at $\ell \sim 120$ represents supergranules. There are no significant features to indicate that either mesogranules ($\ell \sim 600$) or giant cells ($\ell < 30$) are distinctly different from supergranules.

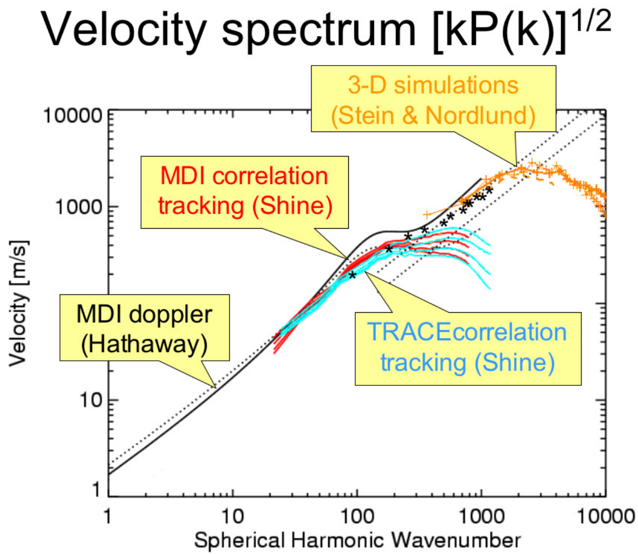

Figure 22: Observed and simulated horizontal velocity amplitudes over a wavenumber range extending from global scales to below granulation scales. Observed velocities are from correlation tracking of TRACE and SOHO white light images (Shine, private communication), and from SOHO/MDI Doppler image modeling (Hathaway *et al.*, 2000, and private communication). Simulation results are from Stein and Nordlund (1998) (granulation scales – orange symbols) and Stein *et al.* (2006a,b) (supergranulation scales – black symbols).

It all began with 8.5 hours of high resolution test Doppler data from MDI on observed on Jan. 27, 1996.   Back in those days, people dressed funny and everyone looked strangely younger than they do today…

The data were analyzed thoroughly. Somebody had the bright idea to use the new technique of time-distance helioseismology to look for supergranules in this very nice dataset.

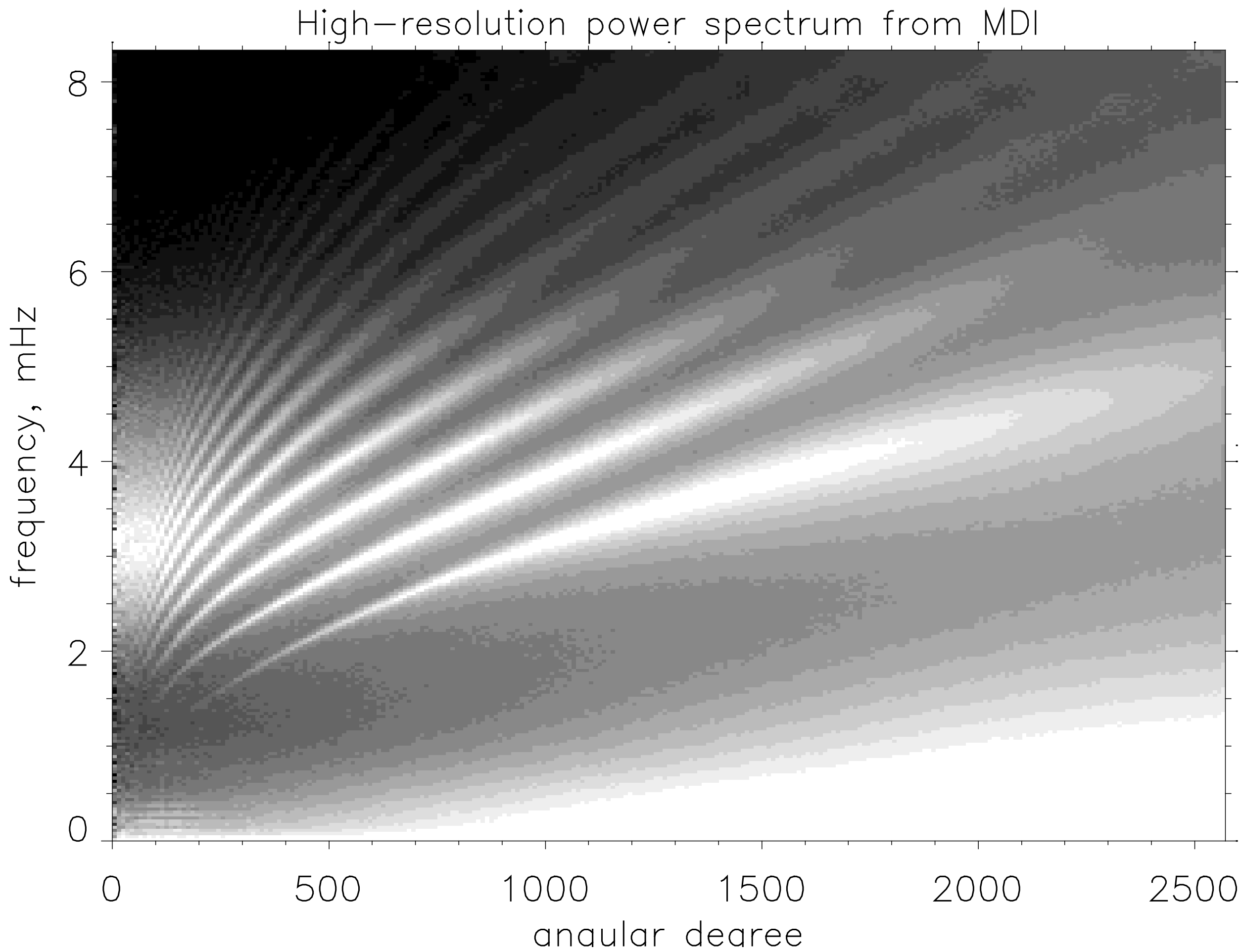

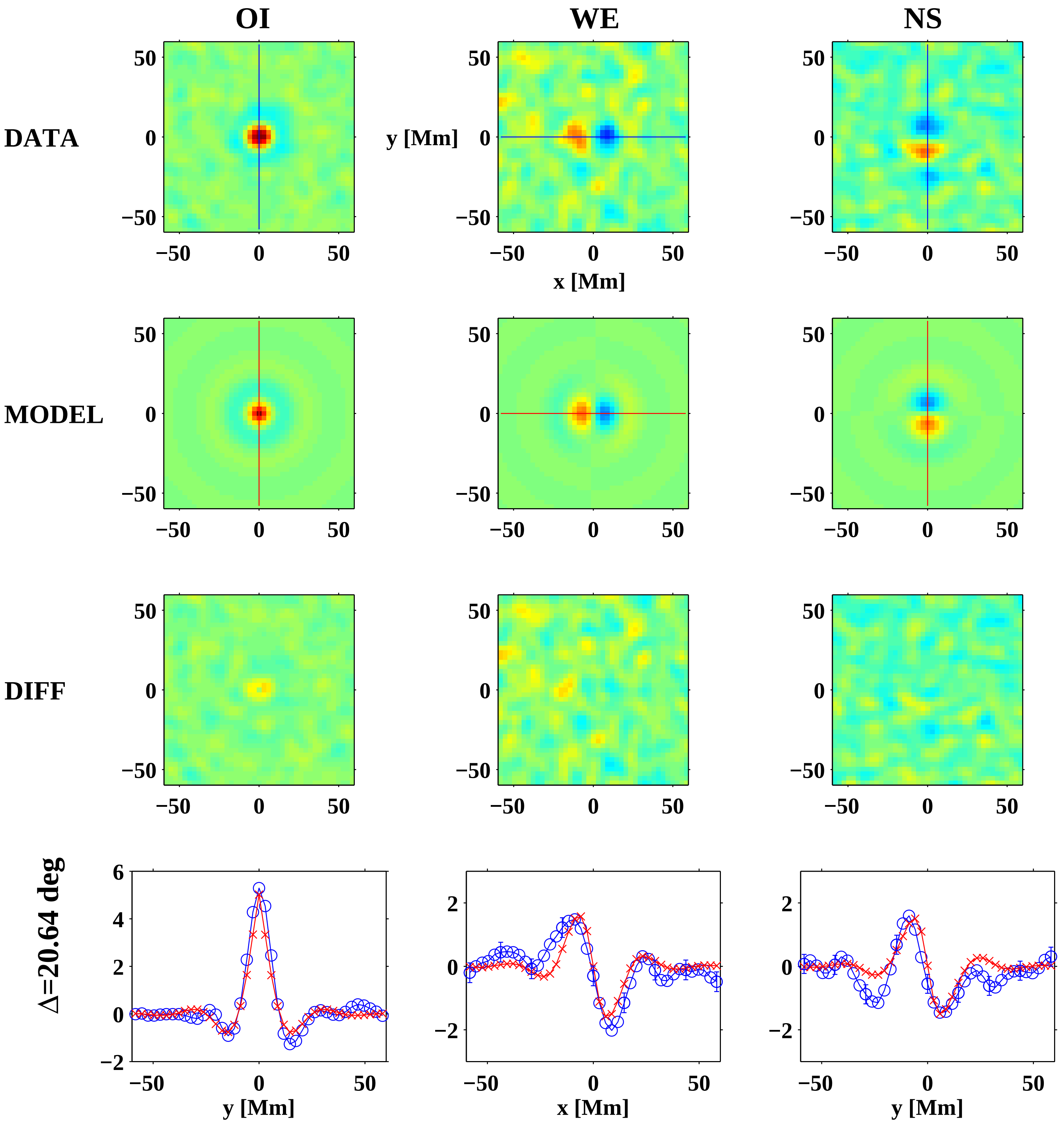

OI
WE
NS
DATA
MODEL
DIFF
Δ=20.64 deg
y [Mm]
x [Mm]
y [Mm]
x [Mm]
y [Mm]

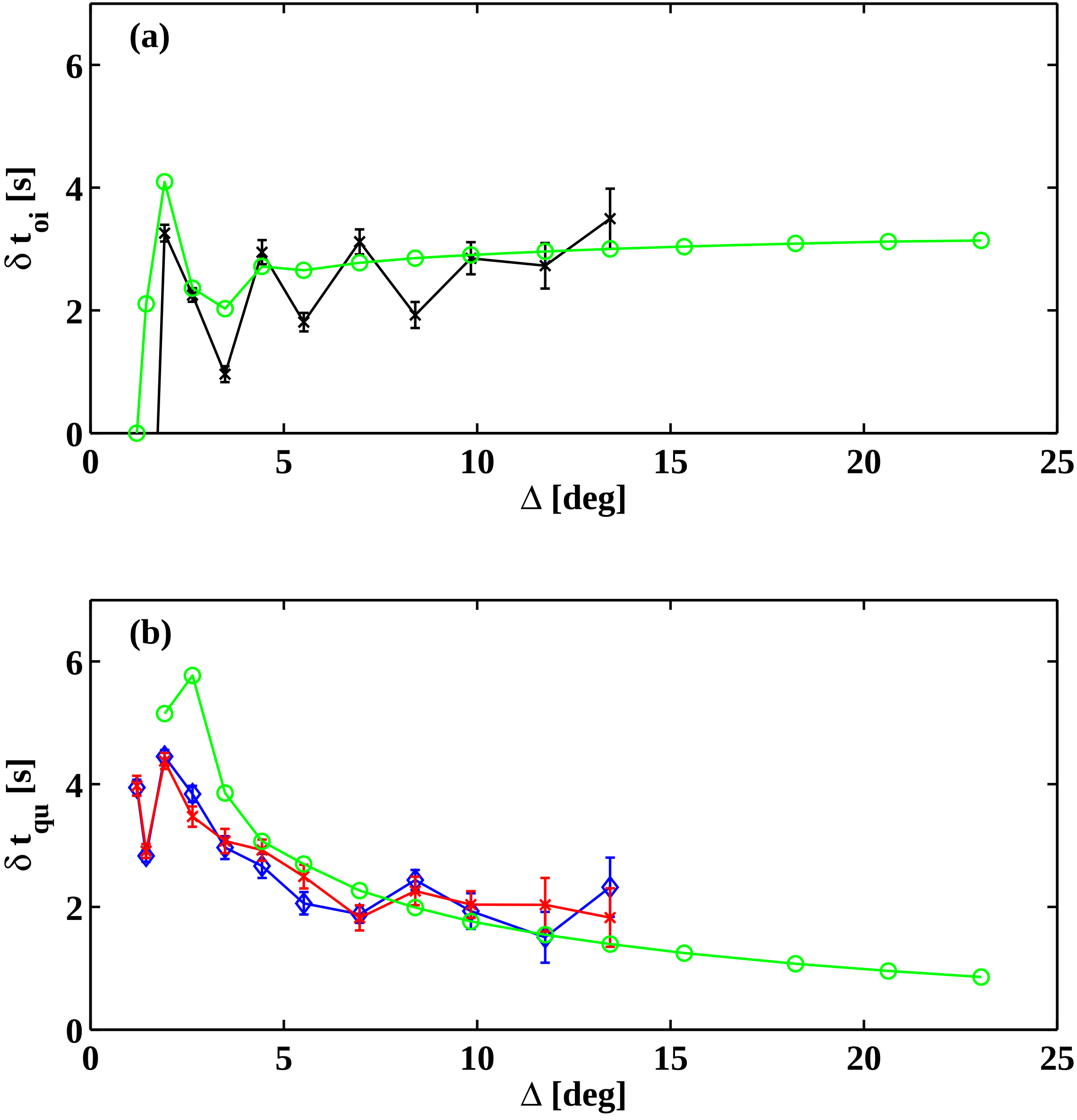
(a)
δ t_oi [s]
Δ [deg]
(b)
δ t_qu [s]
Δ [deg]
0
2
4
6
0
5
10
15
20
25

$$\frac{\partial}{\partial z}(\rho v_z) = -\rho \nabla_{\mathbf{h}} \cdot \mathbf{v_h}, \tag{1}$$

where ρ is the z dependent density, v_z is the z component of velocity, $\nabla_{\mathbf{h}}$ is the horizontal divergence, and $\mathbf{v_h}$ is the horizontal velocity. The model is assumed to separate into horizontal and vertical functions

$$\mathbf{v_h} \equiv -f(z)\mathbf{g}(x, y), \tag{2}$$

$$v_z \equiv u(z)\nabla_{\mathbf{h}} \cdot \mathbf{g}, \tag{3}$$

where $\mathbf{g}(x, y)$ is a vector in the horizontal plane with no units, $f(z)$ has units of velocity, and $u(z)$ has units of velocity times length. Our method of solution is to first specify the horizontal function $\mathbf{g}(x, y)$ and calculate its horizontal divergence $\nabla_{\mathbf{h}} \cdot \mathbf{g}$. The vertical function $u(z)$ is then specified and Equation (1) is used to derive $f(z)$. Some straightforward algebra yields

$$f(z) = \frac{\partial u}{\partial z} + u(z)\frac{\partial \ln \rho}{\partial z}. \tag{4}$$

In general, models are considered with the horizontal function $\mathbf{g}(x, y)$ defined by

$$\mathbf{g}(x, y) = \hat{\mathbf{r}} J_1(kr)e^{-r/R}, \tag{5}$$

where $\hat{\mathbf{r}}$ is the outward radial unit vector in a cylindrical coordinate system, J_1 is the Bessel function of order 1, k is a wavenumber, r is the horizontal distance from the origin, and R is a decay length. k and R are free parameters that will commonly be defined as $k = \frac{2\pi}{30}\,\mathrm{rad\,Mm^{-1}}$ and $R = 15\,\mathrm{Mm}$. This type of horizontal variation was used by Birch and Gizon (2007).

In general models have been considered with a Gaussian z-dependence. v_z is specified at $r = 0$ as a simple Gaussian:

$$v_z(r = 0) = ku(z) = v_0 e^{-(z-z_0)^2/2\sigma_z^2}, \tag{6}$$

where z_0 is the location of the peak of the vertical flow, σ_z is the Gaussian sigma, and v_0 is the maximum vertical flow. To ultimately explain the large-distance travel times, the photosphere needs to be in the far tail of the Gaussian. As the upward flow at cell center is $10\,\mathrm{m\,s^{-1}}$ at the photosphere, this implies a considerably larger vertical flow at depth for the average cell. Values for these parameters that approximate the data are $v_0 = 240\,\mathrm{m\,s^{-1}}$, $z_0 = -2.3\,\mathrm{Mm}$, and $\sigma_z = 0.912\,\mathrm{Mm}$.

2.2. Ray calculations

In the ray theory, the travel time difference for the two directions of propagation through a flow $\mathbf{v}$ is

$$\delta\tau = -2\int_{\Gamma} \frac{\mathbf{v} \cdot \mathbf{ds}}{c^2}, \tag{7}$$

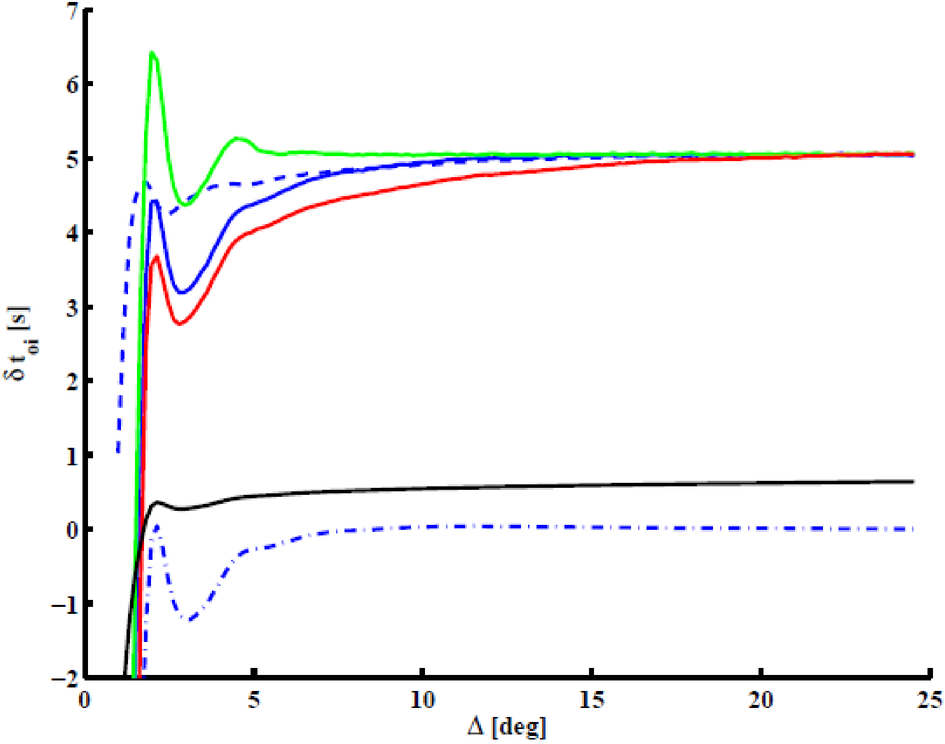

Figure 1. Comparison of various ray models. The blue curves are for the Gaussian model with $z_0 = -2.3\,\mathrm{Mm}$. The dot-dashed blue curve is for the horizontal flow component, the dashed blue curve is for the vertical flow component and the solid blue curve is for the sum. The green curve is for the sum for $z_0 = -1.15\,\mathrm{Mm}$ model and the red curve is for the sum of the $z_0 = -3.45\,\mathrm{Mm}$ model. The solid black curve is the sum for a model with a constant upflow of $10\,\mathrm{m\,s^{-1}}$.

F-mode divergence signal with feature locations overlaid in red.

- Supergranule location: First an f-mode analysis is done to 'find' the supergranules.   Maps of the travel time difference between the inward-going waves and outward-going waves from a central point to an annulus yield a signal proportional to the horizontal divergence. Local peaks in this signal define the location of the centers of the supergranular cells. 64 12-hour intervals were analyzed yielding 60000 supergranules to use.

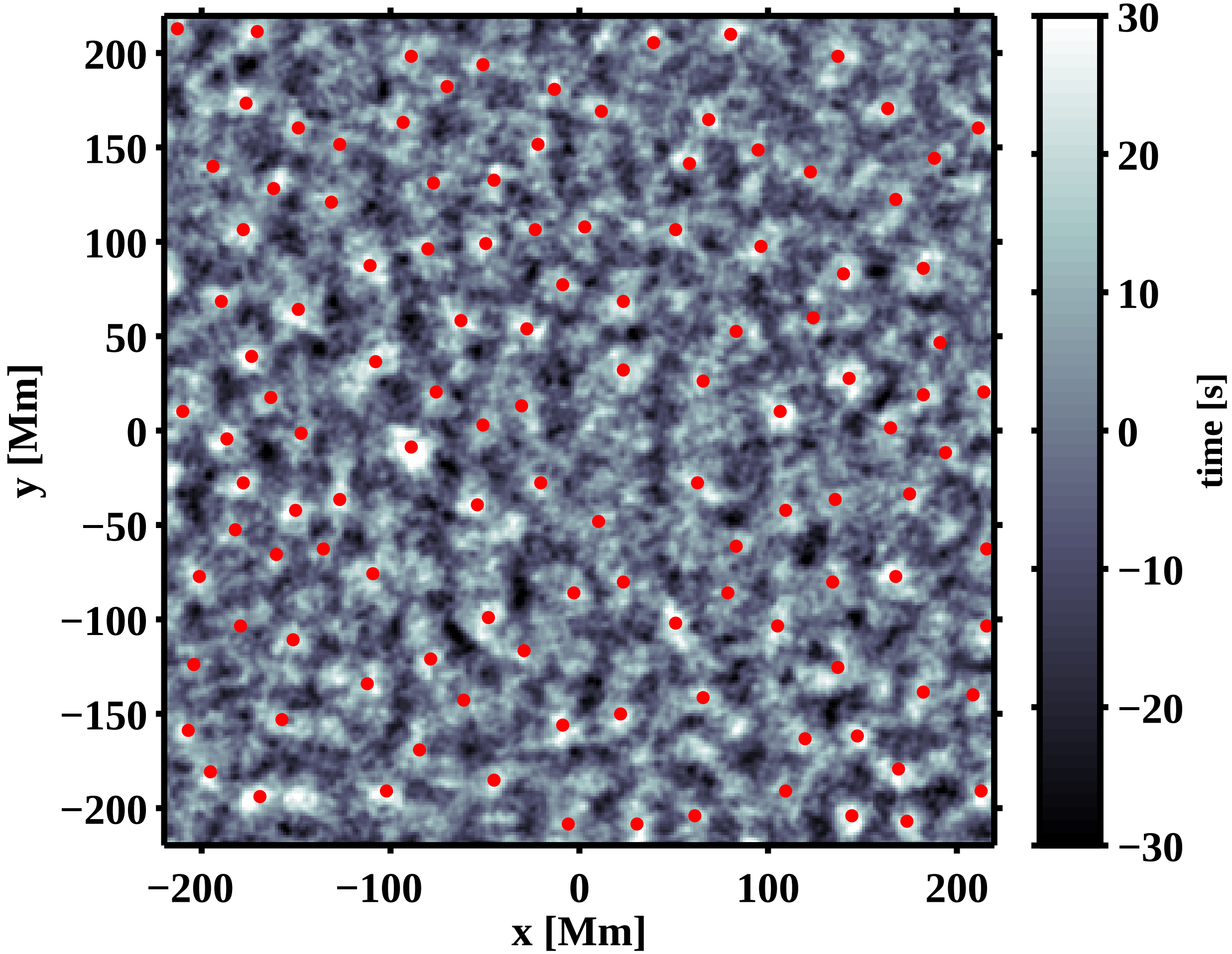

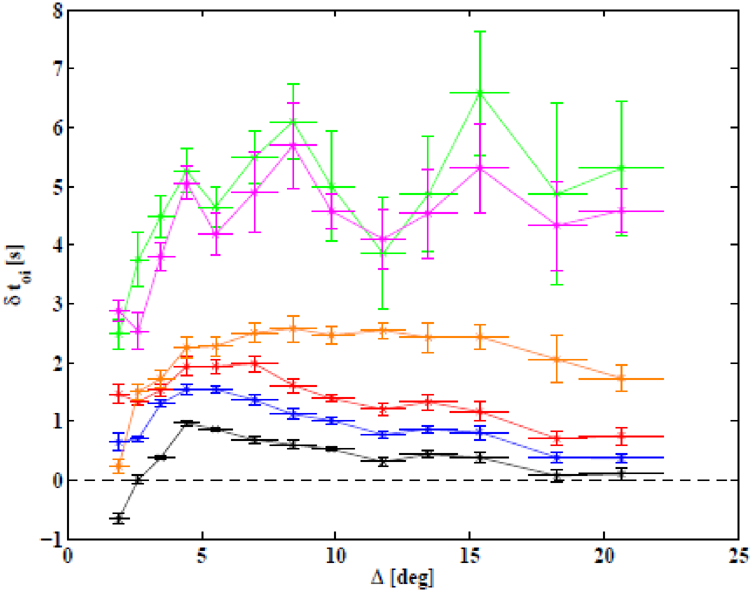

Figure 3. Center-annulus travel time differences δt_{oi} averaged about the supergranule centers for different filters for the thirteen Δ ranges for three days of HMI data. The black points for the the nominal phase speed filters. The blue points are for the phase speed filters with the widths doubled. The red points are for the width tripled. The orange points are for a filter width that is half the nominal phase speed. The green curve is for no phase speed filter. In all cases the f mode is excluded via filtration as is signal outside the frequency bandpass $1.5 < \nu < 6$ mHz. The magenta curve is for the constant degree width filter (Section 3.3) with width $\Gamma_\ell = 400$. These results were obtained using the three days of data 9-11 July 2010.

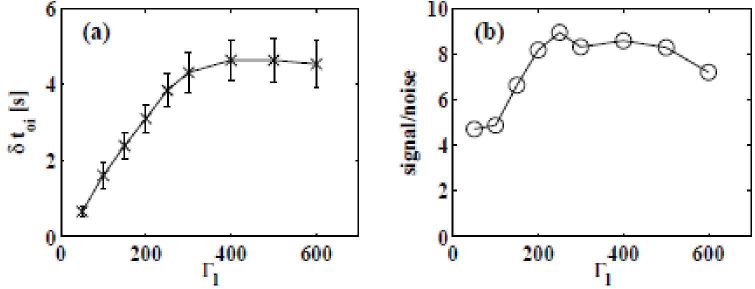

Figure 4. (a) Travel time difference δt_{oi} versus filter FWHM Γ_ℓ. The unfiltered case has $5.3 \pm 1.2 s$. (b) The travel time difference from (a) divided by the size of the error bar from (a) versus the filter FWHM Γ_ℓ. The value for the unfiltered case is 4.6.

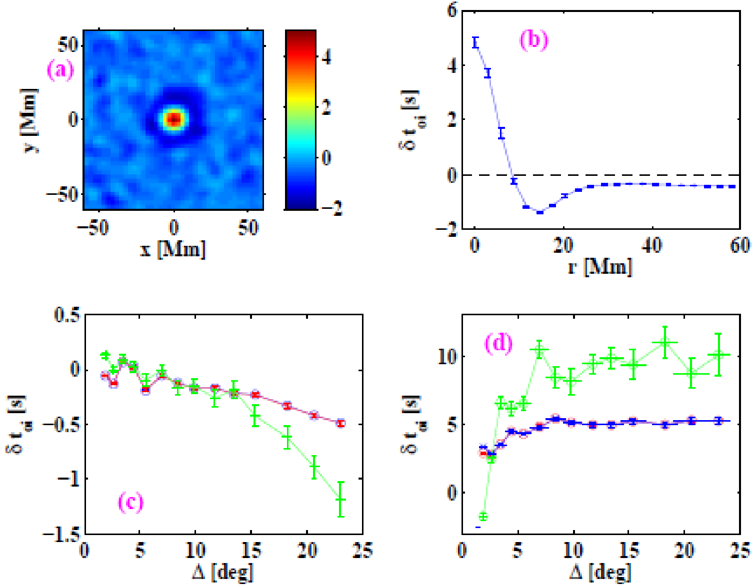

Figure 5. (a) Center-annulus travel time difference averaged about supergranule centers for the range of $\Delta = 22.08\text{–}24\,\mathrm{deg}$. The scale of the colorbar at right is in seconds. Only the central point corresponding to the supergranular center is used in the present study. (b) Azimuthal average of (a). Note the offset at large radii. This offset is believed to be an artifact which needs to be removed from the results. (c) The offset at $r = 58\,\mathrm{Mm}$ for the different travel time definitions versus Δ. Blue is for the Gabor wavelet phase time differences. Red is for the Gizon-Birch phase time differences and the green is for the Gabor wavelet envelope time differences. (d) The resultant travel time differences averaged for the 64 12-hour datacubes corrected for the offset in (c). The colors are the same as in (c).